World Scientific
www.worldscientific.com

Experimental study on oblique water entry of projectiles

Chenggong Zhao*, Cong Wang†, Yingjie Wei‡, Xiaoshi Zhang§ and Tiezhi Sun¶

School of Astronautics, Harbin Institute of Technology,
92 West Dazhi Street, Harbin, Heilongjiang 150001, China
*cgzhhit@gmail.com
†alanwang@hit.edu.cn
‡weiyingjie@gmail.com
§hitzxs@gmail.com
¶sun.tiezhi.hit@gmail.com

An experimental study of oblique water entry of projectiles with different noses has been conducted using high-speed photography technology. The images of the initial water entry impact, cavity evolution, and the closure and shedding of vortices of cavity are presented in the paper. The results reveal that for high-speed oblique water entry (the initial impact velocity > 50 m/s), the cavity attached to the projectile is symmetrical and free from the influence of gravity. The shedding of the water–vapor–air mixture in the tail of the cavity produces vortices which disappear in the rear of the projectile trajectory. Particular attention is given to the velocity attenuation of the projectile after water entry. The results show that there is a transition point at the time corresponding to the surface seal of the cavity during the velocity attenuation after oblique water entry, and the rates of velocity attenuation are different before and after this transition point. Additionally, the chronophotography of the cavity evolution shows that the time when the surface seal of the cavity occurs decreases with the increase of the initial impact velocity of the projectile.

Keywords: Oblique water entry; experiment; projectile; cavity evolution.

1. Introduction

Cavitation occurs in a variety of high-speed hydrodynamic systems where the local pressure controlled by the flow hydrodynamics drops below the saturation pressure of the liquid. In general, cavitation is harmful to hydraulic machinery because it may cause material damage and force surge. However, it is beneficial to reduce

*Corresponding author.

the skin friction drag of underwater vehicle, which in turn enlarges the traveling range of the underwater vehicle.[1] Application of supercavity drag reduction at bullet scales can result in short-range vehicles capable of near sonic to supersonic velocities.[2] These high-speed munitions can be used to defend the mine or torpedo in submarine and surface ship by enhancing the range and ballistic stabilities. The supercavitating hydrodynamics have great influence on the ballistic behaviors and structure dynamics of underwater vehicles.[3]

Experiments on supercavitation formed by water entry projectile can provide crucial data to support the fundamental research of hydrodynamics of supercavitating projectile although projectile water entry has been studied for well over several decades. May and Woodhull[4–6] were among the first to systematically investigate this area. Their early work was based on the related theory regarding seaplane landing floats. One of the most significant applications related to projectile water entry is in the field of military. Air-to-water ballistics for mine clearance and antitorpedo defense require stable water entry at shallow angles of incidence.[7] However, water entry ought to be avoided sometimes, such as in skipping stones.[8] Physical insights of cavity hydrodynamics can also be applied to sports performance research, such as the water entry of athletes, the drag reduction of swimmers near the water–air free surface, the decrease in cavity formation for divers, and the entry and exit of oars in rowing.[9] Experimental work in USA on supercavitating projectile has been carried out mainly at the Naval Undersea Warfare Center (NUWC) in Newport, Rhode Island, and at Pennsylvania State University, State College, PA. The numerous research and development efforts have produced such items as the adaptable high-speed undersea munitions and projectiles for the rapid airborne mine clearance system.[10] However, most of these experimental results have not been published.

Typical experimental methods using high-speed imaging techniques and digital image processing provide effective accesses to study the flow field and ballistic behaviors of water entry problems. The earliest images are those of Worthington and Cole,[11] who captured still images using single spark photography. With the advance of technology, modern high-speed cameras can capture thousands of frames per second (fps) at full resolution and upward of one million frames per second at low resolution. These cameras are capable of fully capturing the unsteady dynamics of the projectile. Extensive high-speed imaging studies of vertical water entry of spheres, projectiles have been presented.[4,6,12–22]

Cavitation number σ, Weber number We, and Froude number Fr are the key parameters used for characterizing the cavitating flow of projectile water entry, which are defined as follows:

$$\sigma = \frac{p_\infty - p_v}{\frac{1}{2}\rho V_0^2}, \tag{1}$$

$$\mathrm{We} = \frac{\rho L V_0^2}{\gamma}, \tag{2}$$

$$\mathrm{Fr} = \frac{V_0}{\sqrt{gL}} \,, \tag{3}$$

wherein p_∞ is the hydrostatic pressure in the ambient liquid and p_v is the saturated vapor pressure of water in local temperature. However, this $(p_\infty - p_v)$ may not represent the actual pressure difference in supercavitating flows of projectile water entry since the cavity pressure may not be equal to the saturated vapor pressure. The numerator of cavitation number, $p_\infty - p_v$, is the pressure difference tending to close the cavity while the denominator, $0.5\rho V_0^2$, is the dynamic pressure tending to resist this closure. In general, supercavitation will be formed when the cavitation number is below approximately 0.1. ρ is the density of liquid and V_0 is the initial velocity of the projectile at the time when the projectile head first hits the water surface. L is the characteristic length and is usually taken as the projectile diameter for the water entry. γ is the surface tension coefficient of liquid and g is the local acceleration of gravity. The Weber number compares the surface tension force with the inertial force, which is especially of importance for microprojectile at low speed. The Froude number indicates the ratio of the inertial force to the gravitational force.

This paper describes design and testing of a laboratory experiment for studying the cavity formed by the oblique water entry of the projectile. The behaviors of the velocity attenuation of free-flying projectile after oblique water entry impact are investigated in this paper. In addition, the relationships between the behaviors of the velocity attenuation and the evolution of the cavity are discussed in the paper. The obtained experimental results can be compared with other results obtained from the simulation of water entry in the related references and can also serve as a reference for modeling the evolution of the cavity using numerical simulations.

2. Experimental Set-up

2.1. *Overview*

The sketch of the experimental set-up is presented in Fig. 1. The set-up consists of four parts: (i) water tank; (ii) launch system; (iii) protective cushion and (iv) imaging system.

2.2. *Water tank*

The water tank consists of an opening top and two pieces of artificial glass on both sides for visualization of the cavity. The scale of the water tank is 1.2 m (width) $\times$ 2.8 m (length) $\times$ 2.4 m (height). It is filled with a volume of water of about 6.7 m^3. Projectiles are fired obliquely along the direction of the launch tube shown in Fig. 1. The front transparent viewing window is mounted on the water tank, which allowed for the capture of supercavities while keeping the high-speed video camera on the exterior of the water tank and reducing the risk of damage to the high-speed video camera due to water splash or projectile fragments. Different from the function of

Light gas gun

Launch tube

Lamp

Compressed nitrogen

Glass
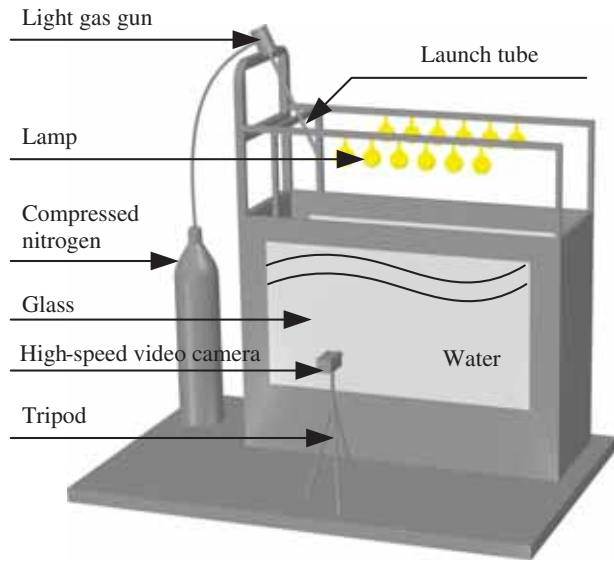
High-speed video camera

Water

Tripod

Fig. 1.   Sketch of the experimental setup.

the front transparent viewing window, the rear transparent window mounted on the water tank is used for light entrance in order for lighting the flow field.

2.3. *Launch system*

The launch system is composed of a light gas gun, a vessel within highly compressed nitrogen and trigger. The projectiles are fired using highly compressed nitrogen as the driven force by the light gas gun. Instead of the fire pin used in general gun, an electronic trigger is used to connect circuits of the solenoid valve, which can release the highly compressed nitrogen to the launch tube and fire the projectile along the direction of the launch tube. Figure 2 shows the photograph of the light gas gun used in the experiments. The light gas gun is fixed on a truss above the water tank and the angle of the launch tube to the water level can be adjusted. In order to maintain synchronization of projectiles and high-speed video camera, the trigger of the light gas gun is synchronized with that of high-speed video camera. The caliber of the light gas gun is 6.1 mm.

2.4. *Protective cushion*

A piece of steel plate is placed at the bottom of the water tank to protect the water tank from damage due to the impact of projectiles. On the top of the steel plate, some pieces of multilayer metal mesh are mounted in order to prevent the bounce of projectiles on the steel plate and recycle projectiles.

Fig. 2.   The photograph of the light gas gun.

2.5. *Imaging system*

Imaging system is critical to the success of the experimental study. The information obtained from those images generated by the imaging system plays an extreme role in data analysis. More importantly, these images are essential to the understanding of the physics of supercavitations.

2.5.1. *The configuration of imaging system*

Imaging system consists of a high-speed video camera *FASTCAM SA6*, a computer, 10 halogen lamps, a trigger of the high-speed video camera, and some supporting structures which are assembled to protect the camera and halogen lamps in case of water splash. The power of each halogen lamp is 1300 W. There are six halogen lamps which were placed at the opposite of the viewing window and a light diffuser was put in front of these halogen lamps. The other four halogen lamps were placed at the top of the water tank. The trigger of the high-speed video camera should be synchronized with the trigger of the light gas gun in order to make the high-speed video camera shoots the projectile and supercavity.

Pictures of the projectile and supercavity during flight were filmed at 5000 fps using the high-speed video camera *FASTCAM SA6*. Halogen lamps were used to illuminate the view in order to make the high-speed video camera capture high-quality pictures. The light was diffused and homogenized by the light diffuser which is made of frosted glass.
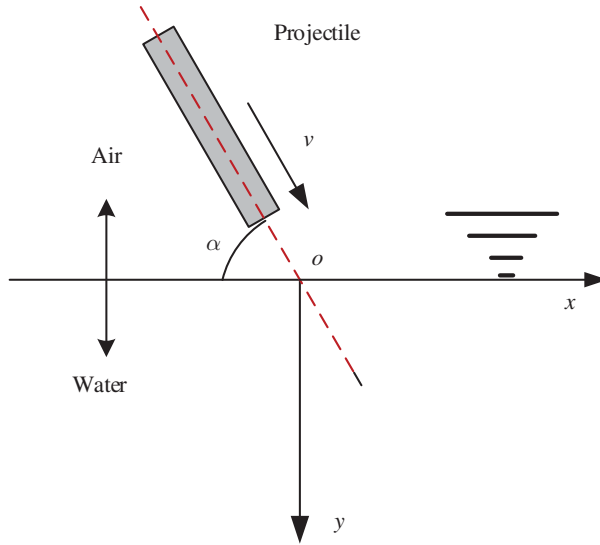
Fig. 3.   Sketch of the coordinate system used for image post-processing.

2.5.2. *Image processing*

Images taken by the high-speed video camera are processed to reveal the trajectory behavior of projectile and the cavity morphology behavior, and also to find clues of the projectile moving stability.

Figure 3 shows the sketch of the global coordinate system used for image post-processing. As shown in the figure, the x-axis is in the horizontal direction and coincides with the water–air free surface. The y-axis is in the direction of gravity. Since the research in this paper is focused on the phase after the water entry of projectiles, the origin of coordinates is made to coincide with the impact point of projectile water entry. The recorded images are transformed to gray level matrices using Matlab. The instant when the projectile first hits the water–air free surface is considered as the initial time $t = 0$ ms, and the corresponding velocity is considered as initial velocity.

The gray level matrices of images can be processed using the Matlab program. Sketch of the program used for image post-processing is shown in Fig. 4. In the figure, each small square represents a pixel of the image and different colors mean the different gray values of the corresponding pixel. From left to right, bottom to top order, the program will check the gray values of each pixel and find the borders which have the maximum gray level gradient. These borders are boundaries of projectiles and cavities and the corresponding coordinates reveal the positions of projectiles and cavities. From the positions of projectiles and cavities, we can obtain the trajectories of projectiles, velocities of projectiles and dimensions of supercavities. The trajectories and cavity measurements are based on the images of the projectile as the scale factor of length and the actual length of projectile
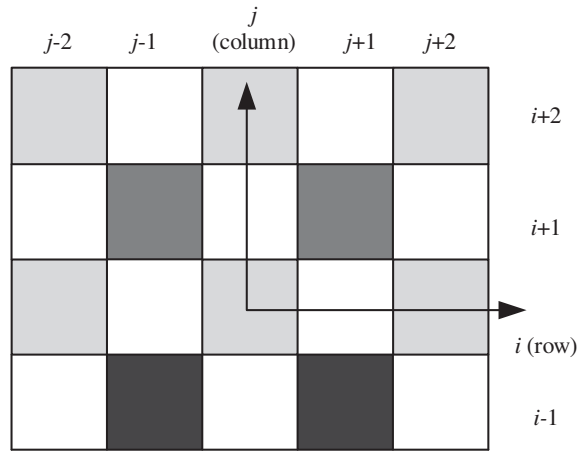
Fig. 4.   Sketch of the program used for image post-processing.

is known from the drawings of projectiles. In addition, the scale factors of the experiments here are identical.

3. Model of Projectile

When a projectile moves through water at sufficient speed after the entry into water, the flow field near the nose of projectile is accelerated in localized regions, which reduces the static pressure below the saturated vapor pressure, causes the vaporization of water, and creates a vapor cavity. In general, the cavity collapses immediately. However, the cavity that will envelop the entire projectile and persist long after the passage of the projectile can be created with sufficient speed and appropriate design, such as a flat nose tip and a larger length to diameter ratio. This phenomenon, called supercavitation, results from the fact that the projectile has only a small wetted nose tip that can reduce the drag dramatically.[2,3] However, the small wetted nose tip results in the instability of the projectile in supercavity. In practice, one way to stabilize the projectile is impingement of the projectile tail on the water–vapor interface. In addition, the impingement forces the projectile back towards the cavity centerline and beyond to the second impingement on the water–vapor interface ultimately. This periodic impingement is named tail-slap which may be caused by the initial yaw–pitch moments or other disturbances.

All projectiles used in tests are made of steel with the same diameter of $D = 6$ mm. The nose shapes of projectiles include flat nose, truncated conical nose, and conical nose. Lengths of flat nose projectiles include $L = 3D$, $6D$, $9D$, $12D$ and $15D$, and the corresponding masses are 3.90, 7.68, 11.49, 15.44, and 19.11 g, respectively. The truncated conical nose projectile and conical nose projectile have the same length of $L = 15D = 90$ mm, and their masses are 18.81 g and 18.69 g,
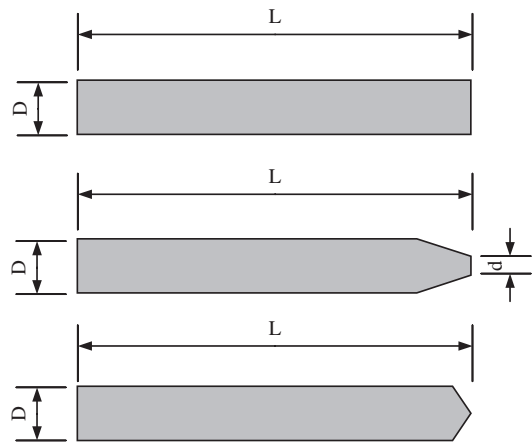
Fig. 5.   Sketch of the projectile dimensions.

Fig. 6.   Projectile photographs.

Table 1.   Geometrical characteristics of projectiles.

	Mass (g)	d (mm)	D (mm)	L (mm)	Taper angle (°)
Flat nose 1	3.90	—	6	18	—
Flat nose 2	7.68	—	6	36	—
Flat nose 3	11.49	—	6	54	—
Flat nose 4	15.44	—	6	72	—
Flat nose 5	19.11	—	6	90	—
Truncated conical nose	18.81	2	6	90	60
Conical nose	18.69	—	6	90	120

respectively. The diameter of the truncated conical nose projectile tip is $d = 2$ mm. In addition, the cone angles are 60° and 120°, respectively. The sketch of the projectile dimensions is shown in Fig. 5. Figure 6 shows the photographs of projectiles and Table 1 gives the geometrical characteristics of the projectiles.

4. Experimental Results and Discussion

4.1. *Initial water entry impact*

The water entry cavities in the first few moments after impact of the projectile are formed and move downward and outward. Figure 7 gives the schematic of projectile water entry obliquely. Here, α denotes the angle of projectile V to the free surface. At the time when the projectile touches the free surface, the jet and the beginning of the cavity are formed.

Two typical impacts are presented in Figs. 8 and 9. Figure 8 illustrates the water entry of projectile model flat nose 3, $L = 54$ mm, $D = 6$ mm, the initial impact velocity is 145.2 m/s (Fr = 599), and the entry angle to the free surface is 65°. Figure 9 gives the chronophotography which presents the evolution of the cavity during the first 4.4 ms after the impact of a projectile model conical nose, $L = 90$ mm, $D = 6$ mm, the initial impact velocity is 53.2 m/s (Fr = 219), and the entry angle to the free surface is 58°. As we know from the research work of Thoroddsen,[20] firstly, for impact cases in which the impact velocity is sufficiently high (Reynolds number, Re > 9000), a small horizontal jet is ejected at great velocity radially outward from the point of contact between the projectile and the liquid surface. The jet formed by the impact can reach speeds up to 30 times the impact speed. The jet forms in less than 1 ms after the impact, is very difficult to capture, and is distinct from the actual splash crown.[9] Surface tension and compressibility appear to have little effect on the formation of the jet.[20] However, from Figs. 8 and 9, we can see that the splash crown and initial radial jet are less pronounced in the water entry obliquely of projectile, compared with that in the water entry vertically of sphere.[13] Due to the insufficient resolution of the high-speed video camera, we can hardly see the first radial jet of the impact.

Using γ for the surface tension of water–air free surface, γD^2 is equal to the order of magnitude of the energy required to perturb the surface over the length scale D of the water–air free surface. According to the principle of energy conservation, the water entry cavity can be created when the kinetic energy of the impact $\sim \rho D^3 V^2$, which is derived from the kinetic energy of the projectile, is more than the surface energy.[13]
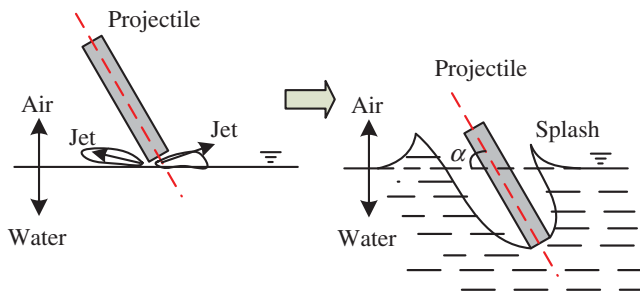

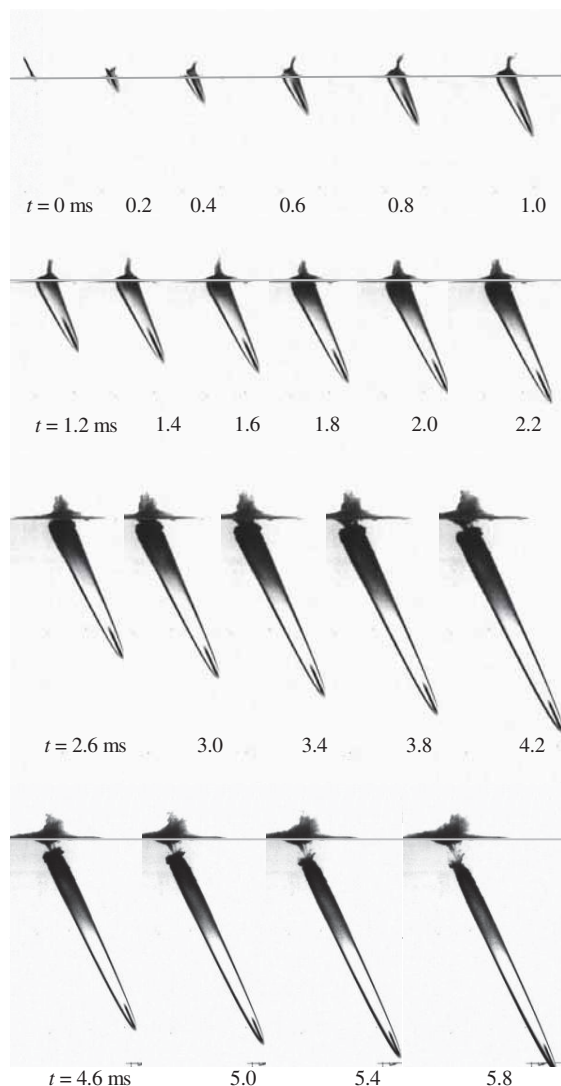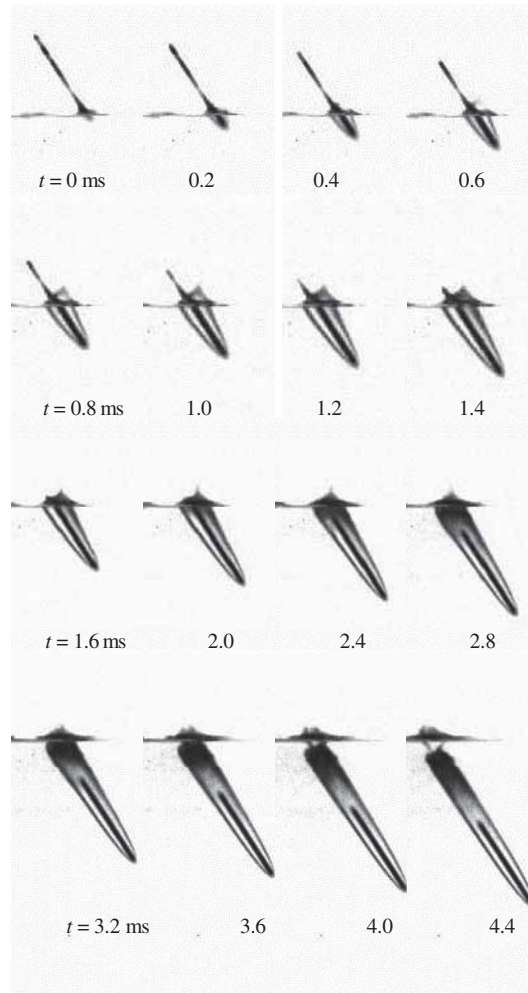Fig. 7.   Schematic of the projectile water entry obliquely.

Fig. 8. The water entry of the projectile model flat nose 3, $L = 54$ mm, the initial impact velocity is 145.2 m/s, and the entry angle to the free surface is 65°.

4.2. Cavity shape

Generally, there are four types of air-entraining cavities that can be formed after water entry of the projectile: surface seal, deep seal, shallow seal, and quasi-static seal.[14] Figure 10 gives the chronophotography of the water entry cavities of the projectile model flat nose 1, $L = 18$ mm and $D = 6$ mm. The initial impact velocity is 235.2 m/s, the entry angle to the free surface is 65°, and Froude number Fr $= 970$. As can be seen in the figure, the type of air-entraining cavities is surface

Fig. 9. The water entry of the projectile model conical nose, $L = 90$ mm, the initial impact velocity is 53.2 m/s, and the entry angle to the free surface is $58°$.

seal. Here, Fr is equal to 970, indicating that the main governing parameter for the cavity seal in Fig. 10 is inertia, rather than gravity.

Focusing on the red color ellipses in Fig. 10, they show the tail-slap of the projectile model flat nose 1. Tail-slap is seen as a blister in the cavity wall. As we can see in the sequence, the tail of projectile protrudes through the cavity wall when tail-slap occurs. The impingement of the projectile tail on the cavity wall which is named tail-slap is a way to stabilize the projectile movement in supercavity.[23] This impingement is mainly caused by the disturbances of projectile when it is launched from air to water. In addition, it cannot be avoided in practice since we cannot avoid the disturbances in the launching phase. Excessive impingement can cause
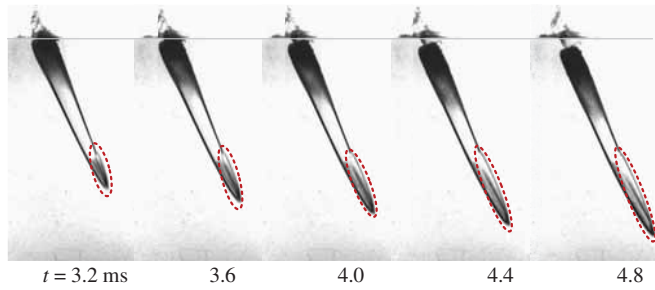
Fig. 10. (Color online) Image sequences showing the cavity shapes and tail-slaps of the projectile model flat nose 1, $L = 18$ mm, the initial impact velocity is 235.2 m/s, the entry angle to the free surface is 65°, and the red color ellipses showing the tail-slap of the projectile.
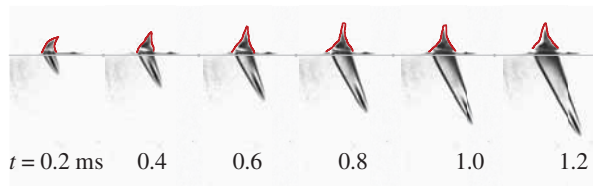
Fig. 11. Image sequences showing the splash dome of the projectile model flat nose 2, $L = 36$ mm, the initial impact velocity is 242.6 m/s, and the entry angle to the free surface is 65°.

the projectile to tumble in water, resulting in the projectile damage and catastrophic failure.

Figure 11 gives the image sequences showing the splash dome of the projectile model flat nose 2, $L = 36$ mm, the initial impact velocity is 242.6 m/s, the entry angle to the free surface is 65°, and the Froude number Fr $= 1000$. Due to the oblique entering, we can see the asymmetry of the splash dome produced by the water entry of the projectile from the first two images in Fig. 11. The splash moves upward and along the direction of the horizontal component of projectile velocity at the same time. Because of the large Froude number of Fr $= 1000$ here, we can see that the cavity attached to the projectile is almost symmetric except for the tail of the cavity. That means, the main parameter here is the inertia and the gravity effect may be neglected.

4.3. *Closure and shedding behaviors of cavity*

The characteristics of closure and shedding behaviors of cavity are shown in Figs. 12 and 13. In these two figures, the projectile model is flat nose 2, $L = 36$ mm, $D = 6$ mm, the initial impact velocity is 242.6 m/s, the entry angle to the free surface is 65°, and the Froude number Fr $= 1000$. After the surface seal of the water entry cavity, the cavity attached to the projectile shrinks due to the pressure difference of ambient pressure and cavity pressure. The projectile exhibits what appears to be re-entrant jet closure.
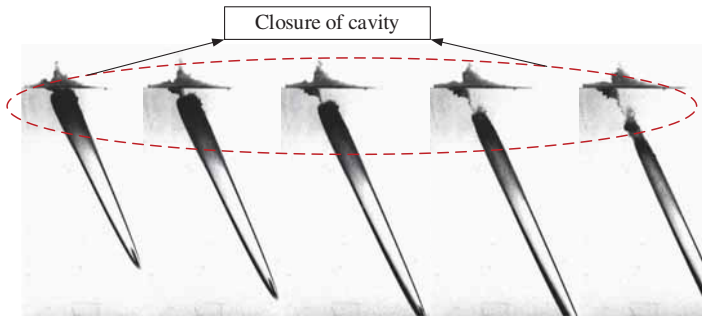
Fig. 12. The closure characteristics of cavity of the projectile model flat nose 2, $L = 36$ mm, the initial impact velocity is 242.6 m/s, and the entry angle to the free surface is 65°.
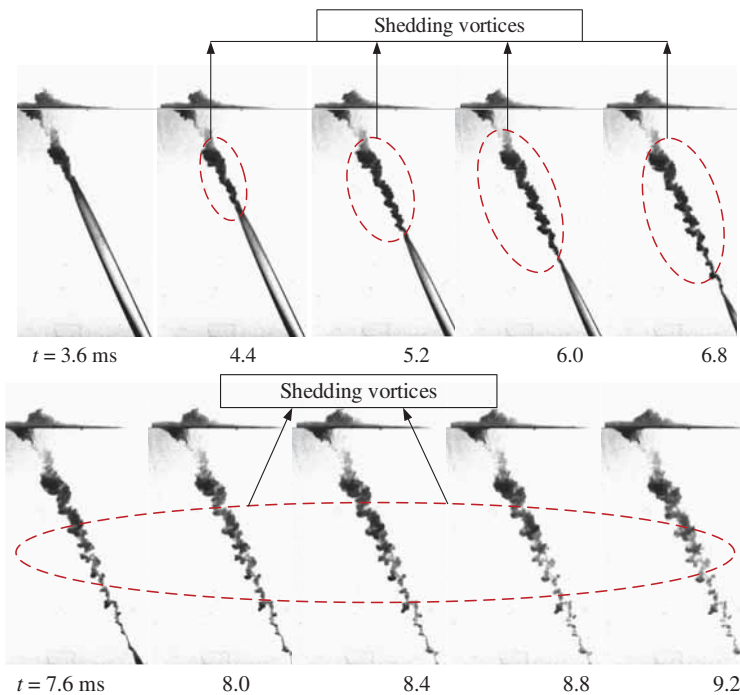

Fig. 13. The shedding vortices characteristics of the projectile model flat nose 2, $L = 36$ mm, the initial impact velocity is 242.6 m/s, and the entry angle to the free surface is 65°.

As shown in Fig. 13, the mixture of vapor and air was condensed to some extent by the high pressure caused due to the severe re-entrant jet. The closure of the cavity is clean and uneventful, leaving a small trail of bubbles consisting of a mixture of water, vapor, and air in the wake that quickly disappeared. The shedding of water–vapor–air mixture produces the vortices which disappear in the rear of the trajectory of the projectile. Regular periods are mainly due to the regular shedding of the vortices caused by the adverse pressure gradient at the cavity closure resulting

from the pressure difference of the ambient pressure and the cavity pressure. The frequency and the amplitude of the shedding vortices decreased over time, which is due to the decrease of the pressure difference of ambient pressure and cavity pressure.

4.4. *Analytical modeling of the dynamics of projectile in supercavitating movement*

The liquid phase does not contact with the moving projectile over most of its length except the tip of the nose, hence the skin drag can be neglected and the drag force of the projectile in water is dominated by the pressure drag component as compared with other items. The drag force is mainly determined by the cavity geometry, nose shape of the projectile, and the velocity of the projectile.

Considering a projectile with an initial velocity V_0 impacting the water–air free surface and along a straight trajectory with the direction of vector **x**. Herein, there are some assumptions: (i) assuming drag coefficient C_x is constant in supercavitating movement of the projectile; (ii) assuming the projectile is intact and does not deform after the water entry impact; and (iii) assuming only the drag force acts on the projectile, that is to say, the gravitational effect of the projectile can be neglected due to the larger Froude number, Fr $\gg 1$. The motion equation of the projectile in supercavity can be obtained from Newton's Law[24]:

$$F = m_p \frac{dV}{dt} = -\frac{1}{2}\rho_1 A C_d V^2 \,, \tag{4}$$

where m_p and V denote the mass and velocity of the projectile, respectively. F stands for the drag force acting on the projectile. A is the characteristic area of the projectile and is defined as the cross-section area. C_d represents the drag coefficient which is associated with the shape of the projectile nose and the initial velocity of projectile.

By integrating Eq. (1), we can get the velocity as a function of time t:

$$V = \frac{1}{Cst + \frac{\rho_1 A C_d}{2m_p}t} \,, \tag{5}$$

where ρ_1 is the water density. Using the initial conditions, $t = 0$, $V = V_0$, and $A = \pi R^2$, we obtain

$$V = \frac{V_0}{1 + \frac{\pi \rho_1 R^2 C_d}{2m_p}V_0 t} = \frac{V_0}{1 + \lambda V_0 t} \,, \tag{6}$$

where R is the radius of the projectile cross-section, λ is the velocity decay coefficient defined as

$$\lambda = \frac{\pi \rho_1 R^2 C_d}{2m_p} \,. \tag{7}$$

Using the initial conditions, $t = 0$, $s = 0$, and integrating Eq. (6), the straight trajectory s of the projectile can be obtained as

$$s = \frac{1}{\lambda} \ln(1 + \lambda V_0 t) \,. \tag{8}$$

From Eqs. (6) and (8), the relation between the projectile velocity and trajectory s can be obtained as

$$V = V_0 \exp(\lambda s).$$

(9)

4.5. *Influence on the velocity decay of the impact velocity V_0 and projectile headform*

The velocity decays at different initial impact velocity values V_0 for the conical nose projectiles at two different water entry angles, 58° and 65°, are presented in Figs. 14 and 16. As can be seen in Figs. 14 and 16, initial velocities of all conical nose projectiles are divided into the ranges of above 100 m/s and below 100 m/s. We can see that all the velocity attenuations of projectiles in these two figures can be divided into two phases. In addition, this characteristic can be found in all the experiments including different initial impact velocities and different water entry angles to the free surface.

As shown in Figs. 14 and 16, each velocity attenuation curve has a transition point which divides the curve into two parts. It is obvious that the rates of velocity attenuation before and after this point are distinct. At the first phase, the rates of velocity attenuation are much less than those of the second phase when the initial impact velocities are below 100 m/s, as shown in Fig. 14. Figure 15 gives the chronophotographies of the cavity evolutions in the vicinity of the transition points for the cases $V_0 = 103$ m/s and 88 m/s in Fig. 14 in which the transition points are at the times $t = 3.4$ ms and 4.0 ms, respectively. As shown in the figure, the surface seals occur at the times $t = 3.4$ ms in Fig. 15(a) and $t = 4.0$ ms in
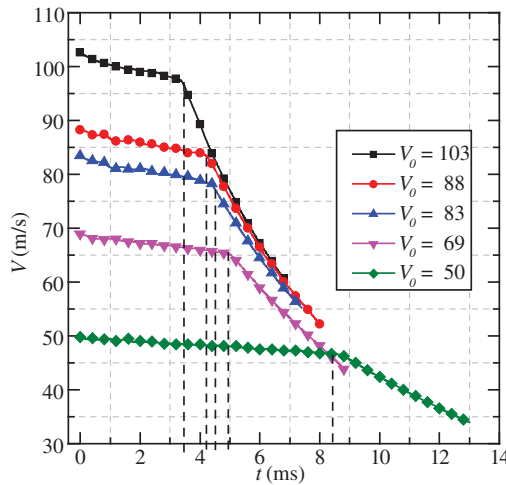
Fig. 14.   (Color online) Influence on the velocity decay of the initial impact velocity V_0, the projectile model is conical nose with $L = 90$ mm, $D = 6$ mm, the entry angle to the free surface is 58°, and the taper angle is 120°.
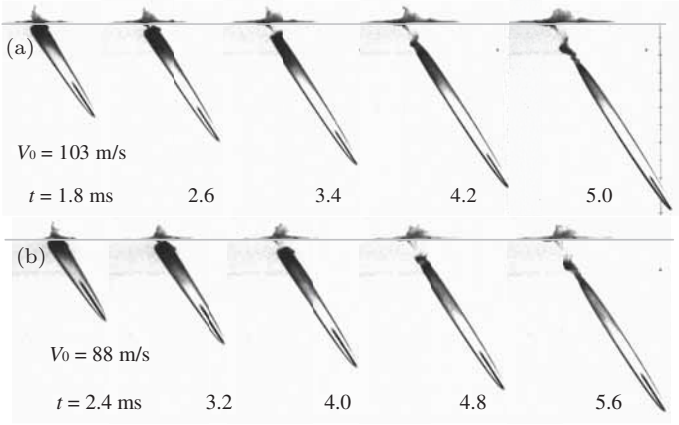
Fig. 15. The cavity evolutions corresponding to the cases $V_0 = 103$ m/s and 88 m/s in Fig. 14 at the times near their transition points. The time step is constant between the images for these two chronophotographies, i.e. $\Delta t = 0.8$ ms.
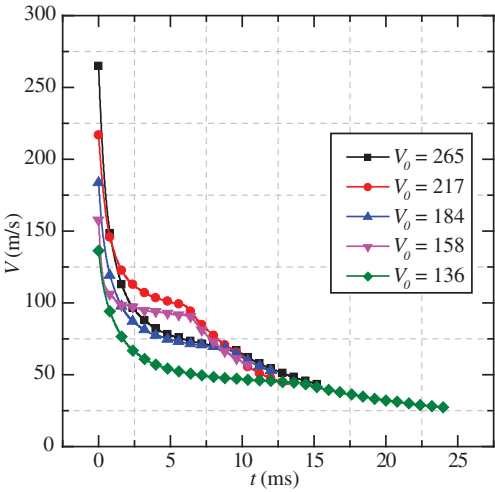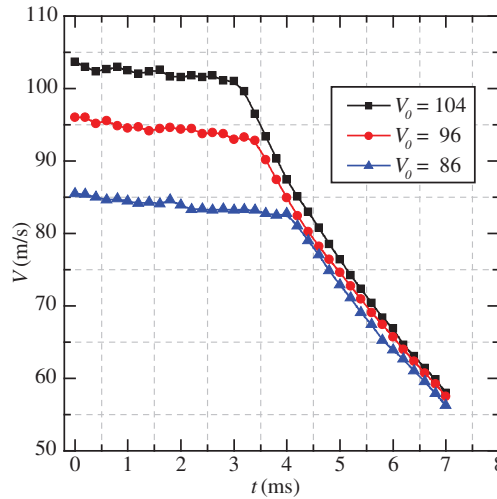

Fig. 16. (Color online) Influence on the velocity decay of the impact velocity V_0, the projectile model is conical nose with $L = 90$ mm, $D = 6$ mm, the taper angle is 120°, and the entry angle to the free surface is 65°.

Fig. 15(b). Before the surface seal, the cavity formed by the projectile is open. The pressure in the cavity is equal to that of the atmosphere, therefore, the cavity number σ is almost equal to zero and the main force acting on the projectile is the skin friction of the projectile head, hence, the rate of velocity decay is much less than that of the second phase. After the surface seal of the cavity, the pressure in the cavity is not equal to the ambient pressure and there is a pressure difference Δp inside and outside the cavity. It is the pressure difference Δp that drives the evolution of the cavity. In the second phase the main forces acting on the projectile

Fig. 17. (Color online) Influence on the velocity decay of the impact velocity V_0, the projectile model is truncated conical nose, $L = 90$ mm, $D = 6$ mm, the taper angle is 60° and the entry angle to the free surface is 58°.
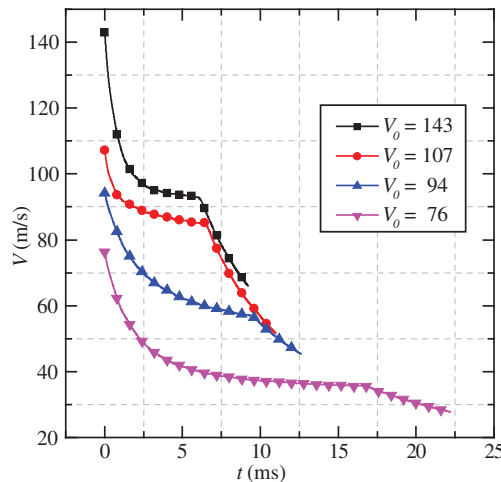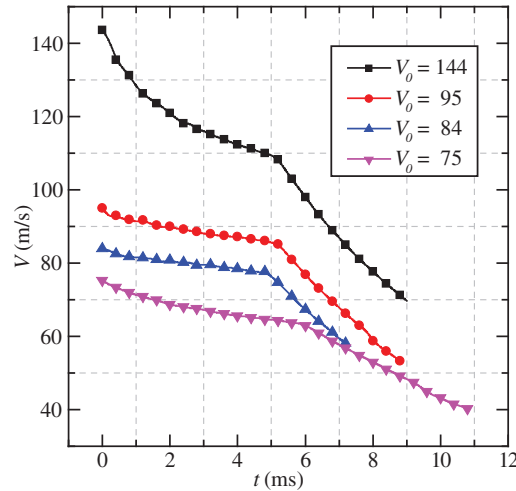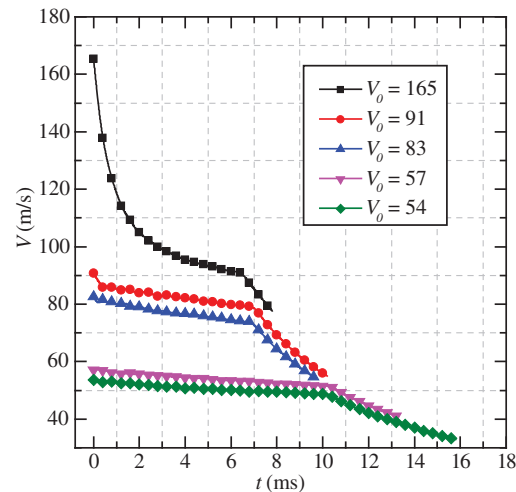

Fig. 18. (Color online) Influence on the velocity decay of the impact velocity V_0, the projectile model is truncated conical nose, $L = 90$ mm, $D = 6$ mm, the taper angle is 60° and the entry angle to the free surface is 65°.

include the skin friction of the projectile head and the pressure resistance due to the pressure difference of the cavity, therefore, the rate of velocity attenuation is higher. Additionally, due to the difference of the forces acting on the projectile in the two phases, the velocity attenuation rates are different before and after the transition point. Comparing Figs. 14 and 16, we can find that the rate of velocity decay is large with the increase of the initial impact velocity and the entry angle to the free surface.
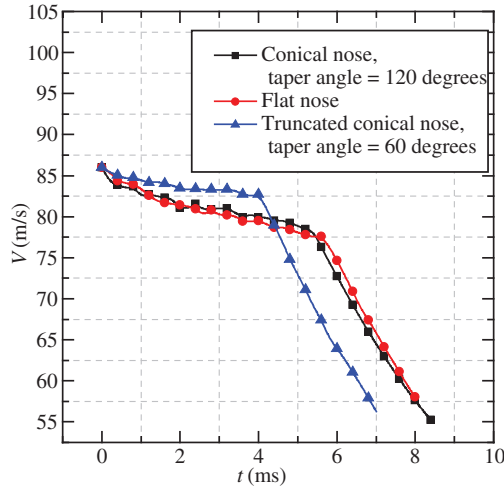
Fig. 21. (Color online) Influence on the velocity decay of the headform, $L = 90$ mm, $D = 60$ mm, the entry angle to the free surface is $58°$, the initial impact velocities are all 86 m/s, the headforms include conical nose, flat nose, and truncated conical nose.

As shown in Fig. 20, the difference of the rates before and after the transition points decreases with the reducing of the initial impact velocity V_0. That is to say, the assumption that the drag coefficient is a constant after the water entry of the projectile can be acceptable when the initial impact velocity V_0 is low enough (< 60 m/s for models of the projectiles used in the experiments).

Figure 21 presents the velocity attenuations influenced by the headforms of the projectiles of the initial impact velocity $V_0 = 86$ m/s at the water entry angle of $58°$. The headforms include conical nose, flat nose, and truncated conical nose. As can be seen in the figure, the velocity attenuations are almost the same for the flat nose projectile and conical nose projectile, however, the velocity attenuation of truncated nose projectile has a relatively large difference compared with those of the flat nose projectile and conical nose projectile. The difference of the times of transition points occurring indicates that the surface seal of the cavity of truncated conical nose projectile occurs first and the surface seal of the cavity of flat nose projectile occurs latest. However, the decelerations of all projectiles with conical nose, flat nose, and truncated conical nose are the same after the transition points.

5. Summary and Conclusions

In this paper, oblique water entry behaviors of cylindrical projectiles with different noses, including flat nose, conical nose, and truncated conical nose, are studied experimentally. Section 2 focused on the key design features of the experimental setup. In addition, the detailed geometric characteristics of the projectiles design were laid out in Sec. 3. The results of the experiments were presented in Sec. 4

and the discussion of the results were presented, too. Within the limitations of the presented study, the following main conclusions can be drawn:

(i) For high-speed oblique water entry (the initial impact velocity > 50 m/s, Froude number > 206), the cavity attached to the projectile is symmetrical and almost free from the influence of gravity.

(ii) After the surface seal of the cavity is formed by the oblique water entry of the projectile, the shedding of water–vapor–air mixture in the tail of the cavity produces the vortices which disappear in the rear of the trajectory of the projectile.

(iii) The velocity attenuation curve of the oblique water entry of the projectile can be divided into two phases by a transition point at the time corresponding to the surface seal of the cavity, and the rates of velocity attenuation are different in these two phases due to different external forces.

(iv) The time at which the surface seal of the cavity occurs decreases with the increase of the initial impact velocity of the projectile.

Acknowledgments

References

1. Yu. N. Savchenko, Control of supercavitation flow and stability of supercavitating motion of bodies, in *Lecture Notes for RTO AVT/VKI Special Course on Supercavitating Flows*, (VKI, Brussels, 2001).
2. J. Hrubes, *Exp. Fluids* **30** (2001) 57.
3. A. May, Water entry and the cavity-running behavior of missiles, Technical Report, US Department of Commerce (1975).
4. A. May, *J. Appl. Phys.* **22** (1951) 1219.
5. A. May, *J. Hydronaut.* **4** (1970) 140.
6. A. May and J. C. Woodhull, *J. Appl. Phys.* **19** (1948) 1109.
7. T. T. Truscott, A. Techet and D. Beal, Shallow angle water entry of ballistic projectiles, in *Proc. 7th Int. Symp. Cavitation*, Ann Arbor, Michigan (ASME, 2009).
8. C. Clanet, F. Hersen and L. Bocquet, *Nature* **427** (2004) 29.
9. T. T. Truscott, B. P. Epps and J. Belden, *Annu. Rev. Fluid Mech.* **46** (2014) 355.
10. P. J. Cameron *et al.*, *J. Fluids Eng.* **133** (2011) 21303.
11. A. M. Worthington and R. Cole, *Philos. Trans. R. Soc. A, Math. Phys. Eng. Sci.* **189** (1897) 137.
12. H. Abelson, *J. Fluid Mech.* **44** (1970) 129.
13. V. Duclaux *et al.*, *J. Fluid Mech.* **591** (2007) 1.
14. J. M. Aristoff and J. W. Bush, *J. Fluid Mech.* **619** (2009) 45.
15. R. Bergmann *et al.*, *J. Fluid Mech.* **633** (2009) 381.

16. A. May and W. R. Hoover, A study of the water-entry cavity, Technical Report, US Department of Commerce (1963).
17. A. May and J. C. Woodhull, *J. Appl. Phys.* **21** (1950) 1285.
18. E. Richardson, *Proc. Phys. Soc. London* **61** (1948) 352.
19. H. H. Shi, M. Itoh and T. Takami, *Trans. ASME, J. Fluids Eng.* **122** (2000) 806.
20. S. Thoroddsen *et al.*, *J. Fluid Mech.* **499** (2004) 139.
21. T. T. Truscott and A. H. Techet, *J. Fluid Mech.* **625** (2009) 135.
22. F. C. Li and C. X. Jiang, *Sci. China: Phys. Mech. Astron.* **9** (2015) 76.
23. Yu. N. Savchenko, Supercavitation: Problems and perspectives, in *4th Int. Symp. Cavition*, Pasadena, CA (CaltechCONF, 2001).
24. H. H. Shi and T. Takami, *Acta Mech. Sin.* **17** (2001) 35.